

Cascading Dark Energy

K. Rezazadeh¹, A. Ashoorioon¹, and D. Grin²

¹*School of Physics, Institute for Research in Fundamental Sciences (IPM),
P.O. Box 19395-5531, Tehran, Iran*

²*Department of Physics and Astronomy,
Haverford College, 370 Lancaster Avenue,
Haverford, PA 19041, United States*

(Dated: August 17, 2022)

The standard cosmological model is in the midst of a stress test, thanks to the tension between supernovae-based measurements of the Hubble constant H_0 and inferences of its values from Cosmic Microwave Background (CMB) anisotropies. Numerous explanations for the present-day cosmic acceleration require the presence of a new fundamental scalar field, as do Early Dark Energy (EDE) solutions to the Hubble tension. This raises the possibility that *multiple* fields cooperatively contribute to the dark energy component in bursts throughout cosmic time due to distinct initial conditions and couplings. Here, this Cascading Dark Energy (CDE) scenario is illustrated through a realization that effectively reduces to a two-field model, with two epochs in which dark energy is cosmologically significant. The model is compared to measurements of the CMB, baryon acoustic oscillations, and observations of Type-Ia supernovae. It is found that this scenario ameliorates the Hubble tension, improving over purely late-time models of dark energy, and improves agreement between the related Rock ‘n’ Roll EDE scenario and galaxy survey measurements of baryon acoustic oscillations.

I. INTRODUCTION

Measurements of the present-day Hubble parameter (the Hubble constant H_0) from supernovae [1, 2] and lensing time delays [3, 4] disagree with the value inferred from the Cosmic Microwave Background (CMB) data [5–7] fit to the Λ CDM model. More specifically, CMB power spectra determined by the *Planck* collaboration yield a best fit value of $H_0 = 67.4 \pm 0.6 \text{ km s}^{-1} \text{ Mpc}^{-1}$ [5]. Similarly, measurements of the acoustic horizon by the Dark Energy Survey (DES), combined with constraints to the baryon density from Big-Bang Nucleosynthesis (BBN) abundances, yield the value $H_0 = 67.4^{+1.1}_{-1.2} \text{ km s}^{-1} \text{ Mpc}^{-1}$ [8].

In contrast, observations of Type-Ia supernovae, tethered to a distance ladder obtained using Hubble Space Telescope (HST) measurements of 70 long-period Cepheids in the Large Magellanic Cloud, imply a substantially different value, $H_0 = 74.03 \pm 1.42 \text{ km s}^{-1} \text{ Mpc}^{-1}$ [9]. This is known as the “Hubble tension”. Although this discrepancy might be caused by systematic effects in the data (though none seem sufficient so far), it could alternatively herald exciting new physics beyond the Λ CDM concordance model.

Many proposals have been suggested to resolve this tension (see, e.g. Refs. [10–21]), some of which (late-time resolutions) invoke modifications to Λ CDM which become important near the current cosmological epoch, others of which cause modifications to the cosmic budget at early times (early-time resolutions, which modify cosmic evolution around or before matter-radiation equality).

Among the proposed late-time resolutions are phantom-like Dark Energy (DE) [22, 23], a vacuum phase

transition [24], interacting DE [25, 26], and modified theories of gravity [10, 27–32]. These scenarios [23, 26, 33] and more model-independent generalizations of them [34–36] are highly constrained by the data, especially by measurements of the Baryon Acoustic Oscillations (BAO) [37–39] in galaxy surveys. Late-time resolutions to the Hubble tension usually suffer from some fundamental shortcomings, such as being a worse fit to CMB data than Λ CDM, fine-tuning issues, inappropriate use of an H_0 prior [40], and conflicts with the ages of globular clusters [41–43], as discussed in Ref. [44].

In most realizations of early-time solutions, the sound horizon is reduced by introducing additional radiation energy density to the matter-energy content of the Universe. Such scenarios are also constrained by BAO and the high- ℓ CMB power spectrum [13, 17, 45–47]. For example, in Early Dark Energy (EDE) scenarios, the Universe contains a component (typically a scalar field) whose behavior is like a cosmological constant prior to a critical redshift preceding matter-radiation equality, and dilutes as fast or faster than radiation [13, 17] subsequently.

Aside from the Hubble tension, there is another disagreement between cosmological data sets, known as the S_8 tension. In particular, the value of $S_8 \equiv \sigma_8 \sqrt{\Omega_m}/0.3$ (where Ω_m is the today’s matter density and σ_8 denotes the variance of matter perturbations within $8\text{Mpc}/h$ today) implied by the CMB (when fit by the Λ CDM model) does not agree with the value inferred from measurements of the amplitude of matter density fluctuations in the late-time Universe [48–54].

Results from Dark Energy Survey (DES) 3-year data yield the constraint $S_8 = 0.797^{+0.015}_{-0.013}$ (68% CL) [54], in contrast with the value $S_8 = 0.832 \pm 0.013$ (68% CL) implied by the best fit value for the amplitude of the scalar

density power spectrum from Planck 2018 TT,TE,EE +lowE+lensing data, assuming Λ CDM [5]. Although EDE models can alleviate the H_0 tension, they tend to exacerbate the S_8 tension [47, 55, 56] and worsen fits to BAO data (see, e.g. [13, 17, 47]).

It is interesting to consider the possibility that these tensions (and the required fine tuning of EDE models) could be alleviated by a richer dark energy sector, for example, if there are multiple epochs of cosmic acceleration driven by one field [57–60], or if many scalar fields acting over time could yield better concordance between cosmological data sets [61].

In this paper, we explore if a resolution for the Hubble tension can be found in the Cascading Dark Energy (CDE) scenario, in which multiple scalar fields contribute to dark energy, analogously to the assisted inflationary scenario [62]. CDE is motivated by recent developments in string theory, such as the swampland conjecture [63–65]. CDE reduces the Hubble tension primarily by altering the early-time sound horizon, like the standard EDE scenario.

Some of the fields, however drop out of sync from the others due to their initial conditions - that is to say that they no longer roll slowly (with nearly constant-energy density) even as other fields jointly continue to behave as dark energy. The evolution of each field becomes significant after the Hubble parameters drop below some specific value which depends on the effective mass of the field as well as the background energy density. After that, the field begins to oscillate around the local minimum of its potential and loses its energy accordingly.

In the simplest realization, our model will reduce to two fields, allowing us to treat the dynamics of each field separately without resorting to an effective one-field approximation, as was done in, e.g. Ref. [61]. Multi-field models for dark energy are well motivated by considerations from string theory, such as the axiverse scenario [66], in which a broad mass spectrum of ultra light axions could contribute to both dark matter and dark energy [67, 68]. They may contribute to explaining the “why now” question for the late-time dark energy driving present day cosmic acceleration [69, 70]. At earlier times, multiple-field scenarios could help reduce the fine tuning needed for EDE models to succeed. Here, we consider the possibility that some dark energy fields are relevant near equality/recombination, while others are more relevant today.

We investigate the behavior of the Hubble parameter and the field configuration in our setup. Both fields couple to gravity minimally, and their kinetic terms are assumed to be canonical. The potentials of both fields in the simplest realization are assumed to be quartic, although one can assume that they are different, as we will explain later. In our work, we check the consistency of the CDE scenario with the existing data, including the CMB [5–7], Pantheon SN [71], BAO [38, 39, 72], and Riess et al. (2019) [9] measurements.

We use the publicly available CosmoMC code [73] in

our investigation to constrain model parameters in light of the experimental data. Using the CosmoMC code, we calculate the χ^2 values for our model for different data sources. To analyze the CosmoMC chains, we apply the GetDist package [74] and a burn-in fraction of 0.3. We compare the CDE scenario with the concordance Λ CDM model, as well as with a single-field canonical scalar field that couples minimally to gravity and has a quartic potential.

Furthermore, we compare our model to the Rock ‘n’ Roll quartic model [15], where there is a cosmological constant and an oscillating scalar field acting as EDE. It is known that in the case of a full $(1 - \cos \theta)^n$ potential (as considered in Refs. [13, 17]), anharmonic deviations from quadratic behavior are important in driving perturbative mode evolution towards behavior that more optimally address the H_0 tension than the Rock ‘n’ Roll scenario. Nonetheless, we compare our CDE scenario to the Rock ‘n’ Roll realization of EDE, as it provides a useful foil for comparing single and multi-field models with similar potentials.

We compare the result of our two-field CDE scenario for H_0 with the results of the Λ CDM model, the single-field DE model, and also the Rock ‘n’ Roll scenario. We want to know if the H_0 tension can be resolved via the CDE framework, and if so, whether it has any advantages. We compare the implied value of S_8 for the empirically allowed parameter space of our model with that of these other models.

We find that the two-field CDE model fits the observational data better than the Λ CDM, single-field DE, and Rock ‘n’ Roll models. The result of our two-field CDE model is more consistent with the Riess et al. (2019) measurement in comparison with the predictions of the Λ CDM and single-field DE models, and hence our model can ameliorate the H_0 tension existing among the cosmological data from different sources. Due to the resemblance of our two-field model to the Rock ‘n’ Roll model with $n = 2$, we contrast our setup with that model too. We find that the predictions of quartic two-field CDE are very close to the Rock ‘n’ Roll model with $n = 2$, although the late-time evolution of the dark energy at late times in our model yields a modestly better fit to the BAO data.

The rest of this paper is structured as follows: In Sec. II, we introduce the CDE model and explain its theoretical motivation. Then, in Sec. III, we explore the two-field realization of the CDE model and present its equations of motion. Subsequently, in Sec. IV, we conduct a Monte Carlo Markov Chain (MCMC) analysis to test a two-field CDE scenario using cosmological data. We present our conclusions in Sec. V, where we also put forward avenues to expand and further test the CDE scenario.

II. SETUP OF CASCADING DARK ENERGY

We consider $N + 1$ scalar fields with quartic monomial potentials, with $1 \ll N$, $V(\phi_i) = \frac{\lambda}{4}\phi_i^4$, $i = 1 \dots N + 1$, with the Lagrangian

$$S = \int \sqrt{-g} d^4x \left[\sum_{i=1}^{N+1} \left(\frac{1}{2} \partial_\mu \phi_i \partial^\mu \phi_i - \frac{\lambda}{4} \phi_i^4 \right) \right]. \quad (1)$$

For simplicity, we have assumed that the quartic couplings of all the fields are the same. In principle, these scalar fields can have different initial conditions. We assume the swampland distance conjecture, under which these fields can at most transverse M_P in the field space before a tower of massless species appears. We thus assume that the initial conditions of all the fields are sub-Planckian. Following the de-Sitter swampland conjecture, we also assume that the relative slope of the potential should not be very flat, yielding the constraint that

$$M_P \frac{V'}{V} \gtrsim c = \mathcal{O}(1). \quad (2)$$

Let us assume that all the first N fields have the same initial conditions, which is different from that of the $(N + 1)$ -th field,

$$\begin{aligned} \phi_1 &= \phi_2 = \dots = \phi_N = \phi_0, \\ \phi_{N+1} &= \chi_0. \end{aligned} \quad (3)$$

Then the effective Lagrangian of ϕ_0 and χ_0 can be written as,

$$\begin{aligned} S = \int d^4x \sqrt{-g} & \left(\frac{N}{2} \partial_\mu \phi_0 \partial^\mu \phi_0 + \frac{1}{2} \partial_\mu \chi_0 \partial^\mu \chi_0 \right. \\ & \left. - N \frac{\lambda}{4} \phi_0^4 - \frac{\lambda}{4} \chi^4 \right). \end{aligned} \quad (4)$$

We introduce the new effective fields, ϕ and χ ,

$$\begin{aligned} \phi &\equiv \sqrt{N} \phi_0, \\ \chi &\equiv \chi_0, \end{aligned} \quad (5)$$

to make the kinetic term of the ϕ_0 field in the Lagrangian canonical, which leads to the Lagrangian

$$\begin{aligned} S = \int \sqrt{-g} d^4x & \left(\frac{1}{2} \partial_\mu \phi \partial^\mu \phi + \frac{1}{2} \partial_\mu \chi \partial^\mu \chi \right. \\ & \left. - \frac{\lambda_\phi}{4} \phi^4 - \frac{\lambda_\chi}{4} \chi^4 \right), \end{aligned} \quad (6)$$

where

$$\begin{aligned} \lambda_\phi &\equiv \frac{\lambda}{N}, \\ \lambda_\chi &\equiv \lambda, \end{aligned} \quad (7)$$

Although the fields ϕ_i , $i = 1 \dots N + 1$, cannot be super-Planckian due to swampland conjecture [64], the fields ϕ can be super-Planckian due to the large dressing factor \sqrt{N} , if $N \gg 1$.

With these initial conditions, the fields can act as dark energy components in our setup. The other notable thing is that if $N \gg 1$, the quartic couplings of the χ field become much larger than the ϕ field, whereas the initial condition for the χ field becomes smaller and in fact sub-Planckian compatible with the swampland conjecture. Due to these, the χ field can play the role of the cascade field in our setup which starts oscillating around its minimum after the Hubble parameter drops below its mass, $\partial_\chi^2 V(\chi)$ and its energy density becomes a substantial part of the background energy density. This will lead to a sudden drop of the comoving sound horizon before the decoupling, which enhances the Hubble parameter respectively today if the angular θ_{MC} parameter is fixed by the CMB experiments.

A similar model could be constructed in the context of multi-giant matrix inflation [75–78]) that uses a concentric multiple stack of D3-branes. In that model, the matrix structure of the coordinates perpendicular to the stack of D3-branes, and the ansatz of the $SU(2)$ generator for three of the orthogonal directions perpendicular to the stacks of D3-branes are used. To exploit the model to describe the late time Universe, with the string coupling $g_s \sim 1$, one has to use a large number of D3-branes, $N \sim 10^{40}$, and then one has to worry about to backreaction effects of the D3-branes on the background geometry. Alternatively, one can assume that that g_s itself is extremely small, say $g_s \sim 10^{-100}$ and further suppression of the quartic couplings of the fields to the observed value to explain the dark energy vacuum density, $\lambda_{\phi,\chi} \sim 10^{-120}$ is achieved via the multiplicity of the D3-branes. Recently in Ref. [79], some of us showed that considering the scalar field non-minimally coupled to gravity with a moderate value of non-minimal coupling, one can reduce the required number of D3-branes to achieve the required number of D3-branes to a reasonable number during inflation. This is something that we hope to pursue in the context of cascading dark energy in the future, but for the purpose of this work, how the bare coupling has taken such small values is out of the scope of this work. Instead, we focus on two minimally coupled scalar fields where their couplings, λ , are already small.

III. THE TWO-FIELD SETUP

In this work, we focus on the two-field realization of the CDE model, which consists of two dynamical scalar fields with canonical kinetic terms. The first Friedmann equation for a flat FRW Universe in this setup takes the

following form

$$H^2 = \frac{1}{3M_P^2} (\rho_m + \rho_r + \rho_\phi + \rho_\chi), \quad (8)$$

where $H = \dot{a}/a$ is the Hubble parameter and $M_P \equiv 1/\sqrt{8\pi G}$ is the reduced Planck mass. Furthermore, ρ_m and ρ_r denote the energy densities of matter and radiation, respectively. The energy densities of the scalar field ϕ and χ are respectively denoted by ρ_ϕ and ρ_χ . It should be noted that in our work, we assume that the neutrinos to be massless, and therefore their contribution is included in the energy density of radiation component. The more general treatment of this setup requires also the inclusion of the massive neutrinos, and this possibility may be taken into account in the future extensions of our scenario.

The energy densities of matter and radiation vary with scale factor as follows

$$\rho_m = \rho_{mi} \left(\frac{a_i}{a} \right)^3, \quad (9)$$

$$\rho_r = \rho_{ri} \left(\frac{a_i}{a} \right)^4, \quad (10)$$

where ρ_{mi} and ρ_{ri} are the energy densities of matter and radiation, respectively, at the initial scale factor a_i that we take it deep inside in the radiation dominated era. We normalize these quantities as follows

$$\tilde{\rho}_{mi} \equiv \frac{\rho_{mi}}{M_P^2 H_0^2}, \quad (11)$$

$$\tilde{\rho}_{ri} \equiv \frac{\rho_{ri}}{M_P^2 H_0^2}, \quad (12)$$

where H_0 is the Hubble parameter today. We express the scale factor of the Universe in terms of the number of e -folds as

$$a = a_i e^N, \quad (13)$$

and hence from Eqs. (9) and (10), we find

$$\rho_m = M_P^2 H_0^2 \tilde{\rho}_{mi} e^{-3N}, \quad (14)$$

$$\rho_r = M_P^2 H_0^2 \tilde{\rho}_{ri} e^{-4N}. \quad (15)$$

The energy densities of the two canonical scalar fields are given by

$$\rho_\phi = \frac{1}{2} \dot{\phi}^2 + V_\phi(\phi), \quad (16)$$

$$\rho_\chi = \frac{1}{2} \dot{\chi}^2 + V_\chi(\chi). \quad (17)$$

We take the potential of both the scalar fields in the

following quartic forms

$$V_\phi(\phi) = \frac{1}{4} \lambda_\phi \phi^4, \quad (18)$$

$$V_\chi(\chi) = \frac{1}{4} \lambda_\chi \chi^4, \quad (19)$$

where λ_ϕ and λ_χ are respectively the self-interaction coupling constants for the ϕ and χ fields. Applying the continuity equations for the energy densities Eqs. (16) and (17), we obtain the equations of motion for ϕ and χ , respectively, as

$$\ddot{\phi} + 3H\dot{\phi} + \frac{dV_\phi(\phi)}{d\phi} = 0, \quad (20)$$

$$\ddot{\chi} + 3H\dot{\chi} + \frac{dV_\chi(\chi)}{d\chi} = 0. \quad (21)$$

Now, following Ref. [80], we introduce the following normalized quantities

$$\begin{aligned} \tilde{H} &\equiv \frac{H}{H_0}, & \tilde{\phi} &\equiv \frac{\phi}{M_P}, & \tilde{\chi} &\equiv \frac{\chi}{M_P}, \\ \tilde{\lambda}_\phi &\equiv \frac{M_P^2}{H_0^2} \lambda_\phi, & \tilde{\lambda}_\chi &\equiv \frac{M_P^2}{H_0^2} \lambda_\chi. \end{aligned} \quad (22)$$

As a result, from Eq. (8), we get

$$\tilde{H}^2 = \frac{4(\tilde{\rho}_{mi} e^{-3N} + \tilde{\rho}_{ri} e^{-4N}) + \tilde{\lambda}_\phi \tilde{\phi}^4 + \tilde{\lambda}_\chi \tilde{\chi}^4}{2(6 - \tilde{\phi}'^2 - \tilde{\chi}'^2)}, \quad (23)$$

where prime denotes the derivative with respect to the e -fold number N . If we take the derivative of both sides of the above equation with respect to N , we obtain

$$\begin{aligned} \tilde{H}' = - \frac{1}{\tilde{H}(6 - \tilde{\phi}'^2 - \tilde{\chi}'^2)} &\left[3\tilde{\rho}_{mi} e^{-3N} + \tilde{\rho}_{ri} 4e^{-4N} \right. \\ &\left. - \tilde{H}^2 (\tilde{\phi}' \tilde{\phi}'' + \tilde{\chi}' \tilde{\chi}'') - \tilde{\lambda}_\phi \tilde{\phi}^3 \tilde{\phi}' - \tilde{\lambda}_\chi \tilde{\chi}^3 \tilde{\chi}' \right]. \end{aligned} \quad (24)$$

Applying the normalized quantities (22) in (20) and (21), we also reach

$$\tilde{\phi}'' = - \frac{\tilde{H}(3\tilde{H} + \tilde{H}') \tilde{\phi}' + \tilde{\lambda}_\phi \tilde{\phi}^3}{\tilde{H}^2}, \quad (25)$$

$$\tilde{\chi}'' = - \frac{\tilde{H}(3\tilde{H} + \tilde{H}') \tilde{\chi}' + \tilde{\lambda}_\chi \tilde{\chi}^3}{\tilde{H}^2}. \quad (26)$$

Inserting these into Eq. (24), and then solving the resulting equation for \tilde{H}' , we arrive at

$$\tilde{H}' = - \frac{1}{6\tilde{H}e^{4N}} \left[3\tilde{H}^2 (\tilde{\phi}'^2 + \tilde{\chi}'^2) e^{4N} + 3\tilde{\rho}_{mi} e^N + 4\tilde{\rho}_{ri} \right]. \quad (27)$$

To eliminate \tilde{H}' in Eqs. (25) and (26), we use the above

equation and hence we will have

$$\ddot{\phi}'' = -\frac{1}{6\tilde{H}^2} \left[e^{-4N} \tilde{\phi}' \left(3e^{4N} \tilde{H}^2 (6 - \tilde{\chi}'^2 - \tilde{\phi}'^2) - 3\tilde{\rho}_{mi}e^N - 4\tilde{\rho}_{ri} \right) + 6\tilde{\lambda}_\phi \tilde{\phi}^3 \right], \quad (28)$$

$$\ddot{\chi}'' = -\frac{1}{6\tilde{H}^2} \left[e^{-4N} \tilde{\chi}' \left(3e^{4N} \tilde{H}^2 (6 - \tilde{\chi}'^2 - \tilde{\phi}'^2) - 3\tilde{\rho}_{mi}e^N - 4\tilde{\rho}_{ri} \right) + 6\tilde{\lambda}_\chi \tilde{\chi}^3 \right]. \quad (29)$$

Eqs. (27), (28), and (29), are basic equations that we will solve in our work to find the background dynamics. To determine the initial conditions, we assume the evolution of the two scalar fields start from the slow-roll regime. Therefore, the first term in Eqs. (20) and (21) can be neglected before the other terms, and these equations simplify as follows

$$3H\dot{\phi}_i + \frac{dV_{\phi_i}(\phi_i)}{d\phi_i} \approx 0, \quad (30)$$

$$3H\dot{\chi}_i + \frac{dV_{\chi_i}(\chi_i)}{d\chi_i} \approx 0, \quad (31)$$

which in turn can be written in terms of e -folds number as

$$\tilde{\phi}' \approx -\frac{\tilde{\lambda}_\phi \tilde{\phi}^3}{3\tilde{H}^2}, \quad (32)$$

$$\tilde{\chi}' \approx -\frac{\tilde{\lambda}_\chi \tilde{\chi}^3}{3\tilde{H}^2}. \quad (33)$$

Besides, in the slow-roll regime, the kinetic terms of ϕ and χ are negligible in comparison with their potentials, and therefore the Friedmann equation (8) can be approximated as

$$H^2 \approx \frac{1}{3M_P^2} [\rho_m + \rho_r + V_\phi(\phi) + V_\chi(\chi)]. \quad (34)$$

If we substitute ρ_m and ρ_r from Eqs. (9) and (10), respectively, into this equation, and then use Eqs. (14), (15), (18), (19), and (22), we reach

$$\tilde{H}^2 \approx \frac{1}{12} \left[4(\tilde{\rho}_{mi}e^{-3N} + \tilde{\rho}_{ri}e^{-4N}) + \tilde{\lambda}_\phi \tilde{\phi}^4 + \tilde{\lambda}_\chi \tilde{\chi}^4 \right]. \quad (35)$$

This equation now can be inserted into Eqs. (32) and (33) to give the initial values of derivative of the two scalar fields with respect to N as

$$\tilde{\phi}'_i \approx -\frac{4\tilde{\lambda}_\phi \tilde{\phi}_i^3}{4(\tilde{\rho}_{mi} + \tilde{\rho}_{ri}) + \tilde{\lambda}_\phi \tilde{\phi}_i^4 + \tilde{\lambda}_\chi \tilde{\chi}_i^4}, \quad (36)$$

$$\tilde{\chi}'_i \approx -\frac{4\tilde{\lambda}_\chi \tilde{\chi}_i^3}{4(\tilde{\rho}_{mi} + \tilde{\rho}_{ri}) + \tilde{\lambda}_\phi \tilde{\phi}_i^4 + \tilde{\lambda}_\chi \tilde{\chi}_i^4}. \quad (37)$$

In this equation, $\tilde{\phi}_i$ and $\tilde{\chi}_i$ refer to the initial values of

the scalar fields at the e -fold number $N_i = 0$. It should be noted that we cannot use Eq. (35) as the initial condition for \tilde{H} , because it leads to self-inconsistency of the differential equations. Instead, in order to prevent this problem, we apply the following relation which follows from Eq. (23),

$$\tilde{H}_i^2 = \frac{4(\tilde{\rho}_{mi} + \tilde{\rho}_{ri}) + \tilde{\lambda}_\phi \tilde{\phi}_i^4 + \tilde{\lambda}_\chi \tilde{\chi}_i^4}{2(6 - \tilde{\phi}_i'^2 - \tilde{\chi}_i'^2)}. \quad (38)$$

For $\tilde{\phi}'$ and $\tilde{\chi}'$ in this equation, we substitute their values from the slow-roll equations (36) and (36), respectively.

To integrate the background equations (27), (28), and (29), we used the 8th-order Runge-Kutta algorithm. Our modified version of CAMB, (which we use with CosmoMC to obtain constraints to the CDE model), is available online¹. In order to ensure that the Universe always remains flat in our code for each set of input parameters, we use the parameter $\tilde{\lambda}_\phi$ as a derived parameter. To determine this parameter numerically, we note that the total density parameter at the present epoch is equal to unity for a flat Universe,

$$\Omega_{m0} + \Omega_{r0} + \Omega_{\phi0} + \Omega_{\chi0} = 1, \quad (39)$$

where the subscript “0” refers to the present time. From this equation, we find

$$\tilde{\lambda}_\phi = \frac{12 - \tilde{\lambda}_\phi \tilde{\chi}_0^4 - 2\tilde{\phi}_0'^2 - 2\tilde{\chi}_0'^2 - 12\Omega_{m0} - 12\Omega_{r0}}{\tilde{\phi}_0^4}. \quad (40)$$

We use a shooting method in our numerical code that tests different values for $\tilde{\lambda}_\phi$ in the above equation for each set of free parameters. After several steps, the code finally finds a suitable value for this parameter that satisfies this equation with enough precision. As a result the parameter $\tilde{\lambda}_\phi$ is treated as a derived parameter in our numerical analysis. By requiring the ϕ field to provide the energy density needed required for a flat universe today, we target scenarios in which the data require χ to act as an EDE field and ϕ to be the present-day DE.

IV. NUMERICAL ANALYSIS

Here, we obtain observational constraints to the CDE model at the level of background dynamics, using recent cosmological data. We use the publicly available CosmoMC computational package [73]. In this work, we use the July 2019 version of CosmoMC. This code uses a Markov Chain Monte Carlo (MCMC) simulation to explore the parameter space of the model, using the Metropolis-Hastings algorithm [73].

¹ <https://github.com/krezazadeh/CAMB-CDE-two-field>

Our parameter space consists of $\{\Omega_b h^2, \Omega_c h^2, \theta_{\text{MC}}, \tau, A_s, n_s, \tilde{\phi}_i, \tilde{\chi}_i, \tilde{\lambda}_\chi\}$, where Ω_b and Ω_c denote the present-day density parameters for baryon and cold dark matter, h is the dimensionless Hubble constant $h \equiv H_0/(100 \text{ kms}^{-1} \text{ Mpc}^{-1})$, θ_{MC} refers to the ratio of the comoving sound horizon at decoupling to the comoving angular diameter distance to the surface of last scattering, τ indicates the optical depth, A_s implies the amplitude of the primordial scalar power spectrum, and n_s is the scalar spectral index. In order to obtain well-behaved sampling as described in Refs. [81] (with helpful formulae in Ref. [82]), the parameter θ_{MC} is varied in CosmoMC. A bisection root finding method is then used to obtain the appropriate H_0 value within the Λ CDM model. Observables are properly computed using our modified version of CAMB.

The parameters $\tilde{\phi}_i$ and $\tilde{\chi}_i$ denote the value of the scalar fields at scale factor a_i taken to be deep inside the radiation-dominated era. The coupling constant $\tilde{\lambda}_\chi$ that is used for the coupling constant of the χ scalar field, is treated as a free parameter in our MCMC analysis, while the parameter $\tilde{\lambda}_\phi$ is a derived parameter, as explained earlier.

The CosmoMC package computes the likelihood of cosmological parameters by including the observational data from various sources. We include the combination of CMB, SNe Ia, BAO, and Riess et al. (2019) data sets in our work, and so multiplying the separate likelihoods for these data sets, the total likelihood will be $\mathcal{L} \propto e^{-\chi^2_{\text{total}}/2}$, where $\chi^2_{\text{total}} = \chi^2_{\text{CMB}} + \chi^2_{\text{SN}} + \chi^2_{\text{BAO}} + \chi^2_{\text{Riess2019}}$ encodes the deviation between the observational and theoretical results. Following Refs. [13, 17, 46, 47], we terminate our MCMC analysis when the Gelman-Rubin convergence criterion [83] fulfills $R - 1 < 0.1$. For the statistical analysis of the MCMC chains generated by CosmoMC, we use the publicly available GetDist package [74].

To establish priors for CDE parameters in our MCMC as well as an initial guess for the best fit value, we begin by finding rough initial guesses for $\tilde{\chi}_i$, $\log(\tilde{\phi}_i)$, and $\log(\tilde{\lambda}_\chi)$ that reproduce published Rock ‘n’ Roll *Planck* values for H_0 , redshift of peak CDE energy-density fraction z_c , peak CDE energy density-fraction $f(z_c)$, and Ω_Λ , when numerically integrated using the equations in Sec. III. We then obtain an initial estimate of best-fit parameters for Λ CDM + CDE parameters using a simple random-walk simulation. We begin by choosing standard (but relatively broad) flat priors for the usual cosmological parameters, centered around Planck 2018 best fit values [5], as well as a trial range for CDE parameters: $\Omega_b h^2 \in [0.022, 0.023]$, $\Omega_c h^2 \in [0.115, 0.124]$, $\theta_{\text{MC}} \in [1.02, 1.06]$, $\tau \in [0.02, 0.09]$, $n_s \in [0.959, 0.974]$, $\ln A_s \in [3.019, 3.075]$, $\tilde{\chi}_i \in [0.4, 0.8]$, and $\tilde{\lambda}_\chi \in [14.5, 15.5]$. An initial guess is made for CDE parameters $\log \tilde{\phi}_i$, $\tilde{\chi}_i$, $\log \tilde{\lambda}_\chi$ as well as Λ CDM parameters, and used to compute the likelihood for the full data set (see below) computed within CosmoMC.

Random guesses are subsequently made for all 8 parameters, but kept only if they improve the model likeli-

hood, with a maximum of 100 iterations. The results are insensitive to the values/ranges initially chosen for $\log \tilde{\phi}_i$ and $\log \tilde{\lambda}_\chi$, and indicate a preferred value for $\tilde{\chi}_i \simeq 0.48$. We then use the same flat priors on Λ CDM parameters and final simulation values to initialize a proper likelihood minimization within CosmoMC, whose initial values are used for the subsequent MCMC. A similar procedure was used for the Rock ‘n’ Roll and Single-field DE models considered. We verified that the posterior probability distributions for $\log \tilde{\phi}_i$ and $\log \tilde{\lambda}_\chi$ are nearly as flat as the priors, justifying their use without loss of generality. The initial field value $\tilde{\chi}_i$ is well constrained in our MCMC and contained in the assumed prior.

We incorporate the Planck 2018 CMB data for the temperature and polarization at small (TT,TE,EE) and large (lowl+lowE) angular scales [5, 6]. We additionally take into account the CMB lensing potential power spectrum measured in the multipole range $40 \leq \ell \leq 400$ [7]. The acoustic peaks are affected by the physics of the decoupling epoch, and their locations are sensitive to physical processes occurring between the decoupling epoch and today.

Type Ia supernovae are standardizable candles that have approximately the same absolute magnitude, once corrections for the width of their light curve are applied. Therefore, they are a powerful tool that can be used to probe the expansion history of the Universe. In our MCMC analysis, we use the Pantheon SN sample [71], which consists magnitude measurements for 1048 SNe Ia with redshifts $0.01 < z < 2.3$.

The baryonic acoustic oscillation standard ruler provides a measurement of the angular diameter distance as a function of the cosmological redshift. BAO data can be used to constrain dark energy models. The pressure waves arising from the cosmological inhomogeneities in the baryon-photon primordial plasma affect CMB anisotropies and observations of the Large-Scale Structure (LSS) of the galaxy density field. The peak appearing in measurements of the large-scale galaxy correlation function is caused by BAOs. In our analysis, we use BAO measurements from the the Baryon Oscillation Spectroscopic Survey (BOSS) [39] ($z \simeq 0.15$), the SDSS Main Galaxy Sample [38] ($z \simeq 0.15$), and the 6dFGS [72] ($z \simeq 0.11$).

Finally, we include the Riess et al. (2019) determination of $H_0 = 74.03 \pm 1.42 \text{ km s}^{-1} \text{ Mpc}^{-1}$ [9] for the Hubble constant, based on 70 Cepheid observations in the LMC and observations of nearby Type-Ia supernovae. This determination is an independent constraint of the expansion rate of the local Universe in our computations.

The resulting best fit values and 68% confidence limit (CL) constraints for the parameters of the investigated models are shown in Table I. In the table, we see that the results for our single-field DE model are very close to Λ CDM, and the results of the two-field CDE model are very close to those of the Rock ‘n’ Roll scenario. We also see that both the Λ CDM and single-field DE models return the 68% CL constraint for the present-day Hubble

TABLE I. The best fit values and 68% CL constraints for the parameters of the investigated models.

Parameter	Λ CDM		Single-field DE		Rock ‘n’ Roll		Two-field CDE	
	best fit	68% limits	best fit	68% limits	best fit	68% limits	best fit	68% limits
$\Omega_b h^2$	0.0226089	0.02251 ± 0.00013	0.0225312	0.02251 ± 0.00013	0.0228385	0.02280 ± 0.00015	0.0227861	0.02282 ± 0.00016
$\Omega_c h^2$	0.11827	0.11849 ± 0.00090	0.118691	0.11851 ± 0.00087	0.121385	$0.1222^{+0.0011}_{-0.0014}$	0.122667	$0.1222^{+0.0012}_{-0.0015}$
$100\theta_{\text{MC}}$	1.04116	1.04116 ± 0.00029	1.04108	1.04113 ± 0.00029	1.03951	$1.03942^{+0.00060}_{-0.00042}$	1.0396	$1.03939^{+0.00063}_{-0.00043}$
τ	0.0596178	0.0568 ± 0.0071	0.0572416	$0.0566^{+0.0064}_{-0.0072}$	0.054335	0.0529 ± 0.0071	0.0492794	0.0532 ± 0.0072
$\ln(10^{10} A_s)$	3.04763	3.046 ± 0.014	3.04411	$3.046^{+0.013}_{-0.014}$	3.04998	3.046 ± 0.014	3.04385	3.046 ± 0.014
n_s	0.968599	0.9690 ± 0.0037	0.969799	0.9688 ± 0.0036	0.968158	0.9688 ± 0.0037	0.967781	0.9691 ± 0.0037
$\log(\tilde{\phi}_i)$	—	—	1.81705	$2.56^{+1.3}_{-0.57}$	—	—	3.13425	> 1.76
$\tilde{\chi}_i$	—	—	—	—	0.480162	< 0.523	0.484908	$0.502^{+0.033}_{-0.096}$
$\log(\tilde{\lambda}_\chi)$	—	—	—	—	15.3182	—	15.4771	—
H_0	68.7567	68.60 ± 0.41	68.5669	68.60 ± 0.41	70.9546	$70.94^{+0.58}_{-0.84}$	70.5298	$70.95^{+0.61}_{-0.85}$
Ω_m	0.297999	0.7003 ± 0.0052	0.300383	0.2997 ± 0.0051	0.286467	0.2883 ± 0.0057	0.292401	0.2883 ± 0.0058
Ω_{DE}	0.702001	0.2997 ± 0.0052	0.699617	0.7003 ± 0.0051	0.713533	0.7117 ± 0.0057	0.707599	0.7117 ± 0.0058
σ_8	0.820063	0.8208 ± 0.0060	0.821043	0.8208 ± 0.0058	0.839236	$0.8417^{+0.0072}_{-0.0087}$	0.841436	$0.8415^{+0.0075}_{-0.0087}$
S_8	0.817324	0.820 ± 0.010	0.821567	0.8204 ± 0.0098	0.820089	0.825 ± 0.010	0.830711	0.825 ± 0.010
Age/Gyr	13.7303	13.741 ± 0.019	13.7235	13.739 ± 0.020	13.4444	$13.43^{+0.10}_{-0.049}$	13.4573	$13.43^{+0.11}_{-0.049}$
$\log(\tilde{\lambda}_\phi)$	—	—	-6.34384	$-9.3^{+4.1}_{-4.8}$	—	—	-11.6081	-8.5 ± 3.7

TABLE II. The best fit value of χ^2 for each model and each data set. The χ^2 values corresponding to different CMB measurements including the Planck lensing power spectrum reconstruction (χ^2_{lensing}), baseline high- ℓ Planck power spectra (plik cross-half-mission, $30 \leq \ell \leq 2508$) (χ^2_{plik}), low- ℓ Planck temperature ($2 \leq \ell \leq 29$) (χ^2_{lowl}), and low- ℓ HFI EE polarization ($2 \leq \ell \leq 29$) (χ^2_{small}), are also presented in the table. The table furthermore includes the values of χ^2_{tot} and $\Delta\chi^2 = \chi^2_{\text{Model}} - \chi^2_{\Lambda\text{CDM}}$.

Parameter	Λ CDM		Single-field DE		Rock ‘n’ Roll		Two-field CDE	
	best fit	68% limits	best fit	68% limits	best fit	68% limits	best fit	68% limits
χ^2_{lensing}	8.68279	9.10 ± 0.55	9.10419	9.08 ± 0.50	9.44935	9.89 ± 0.95	9.83209	9.88 ± 0.94
χ^2_{plik}	2348.84	2359.6 ± 5.8	2352.99	2359.7 ± 6.0	2350.28	2360.8 ± 5.8	2348.35	2360.8 ± 5.8
χ^2_{lowl}	23.041	22.91 ± 0.76	22.028	22.93 ± 0.73	22.768	23.34 ± 0.82	23.4205	23.29 ± 0.80
χ^2_{small}	397.156	397.2 ± 1.9	395.741	397.2 ± 1.8	395.778	396.6 ± 1.3	395.745	396.7 ± 1.3
χ^2_{CMB}	2777.72	2788.9 ± 5.9	2777.19	2788.9 ± 6.0	2777.13	2790.7 ± 6.1	2777.35	2790.7 ± 6.0
χ^2_{SN}	1034.74	1034.792 ± 0.083	1034.74	1034.80 ± 0.12	1035.07	1035.05 ± 0.29	1034.82	1035.05 ± 0.32
χ^2_{BAO}	5.77561	5.89 ± 0.81	5.44215	5.86 ± 0.82	8.63314	8.4 ± 2.2	6.61057	8.4 ± 2.2
$\chi^2_{\text{Riess2019}}$	13.7907	14.7 ± 2.2	14.8014	14.7 ± 2.2	4.69061	5.0 ± 2.1	6.07593	5.0 ± 2.2
χ^2_{total}	3832.03	—	3832.17	—	3825.52	—	3824.86	—
$\Delta\chi^2$	0.0	—	0.14	—	-6.51	—	-7.17	—

parameter as $H_0 = 68.60 \pm 0.41 \text{ km s}^{-1}\text{Mpc}^{-1}$, which disagrees with the value $H_0 = 74.03 \pm 1.42 \text{ km s}^{-1}\text{Mpc}^{-1}$ measured by Riess et al. (2019) [9].

The Rock ‘n’ Roll and two-field CDE models yield a best fit value for H_0 of $H_0 = 70.94^{+0.58}_{-0.84} \text{ km s}^{-1}\text{Mpc}^{-1}$ and $H_0 = 70.95^{+0.61}_{-0.85} \text{ km s}^{-1}\text{Mpc}^{-1}$, respectively. These ranges are similar to one other and also in much better agreement with the Riess et al. (2019) measurement than models with no EDE, reducing the H_0 tension appreciably.

Despite this, we see in Table I that the Rock ‘n’ Roll and two-field CDE scenarios predict higher values for the S_8 parameter compared with the Λ CDM and single-field DE frameworks, and hence their results show more deviations from the DES 3-year observations [54], which indicate that $S_8 = 0.832^{+0.015}_{-0.013}$. Therefore, the Rock ‘n’

Roll and two-field CDE scenarios worsen the S_8 tension compared with the Λ CDM and single-field DE setups, a common shortcoming of EDE models [13, 17, 45–47].

In Table I, we also show results for the age of Universe in all the models considered here. The Rock ‘n’ Roll and two-field CDE models result in lower values for the age of Universe than the Λ CDM and single-field DE models, agreeing more closely with the value $t_U = 13.5 \pm 0.15 \text{ (stat.)} \pm 0.23 \text{ (syst.)}$ (± 0.27 by regarding statistical and systematic uncertainties in quadrature) inferred using a sample of old globular clusters [41–43].

In Table II, we present χ^2 values for different models with respect to each data set. We see that the single-field DE model performs comparably to Λ CDM. The Rock ‘n’ Roll and two-field CDE models fit the CMB data better than the standard cosmological model. The Rock ‘n’ Roll

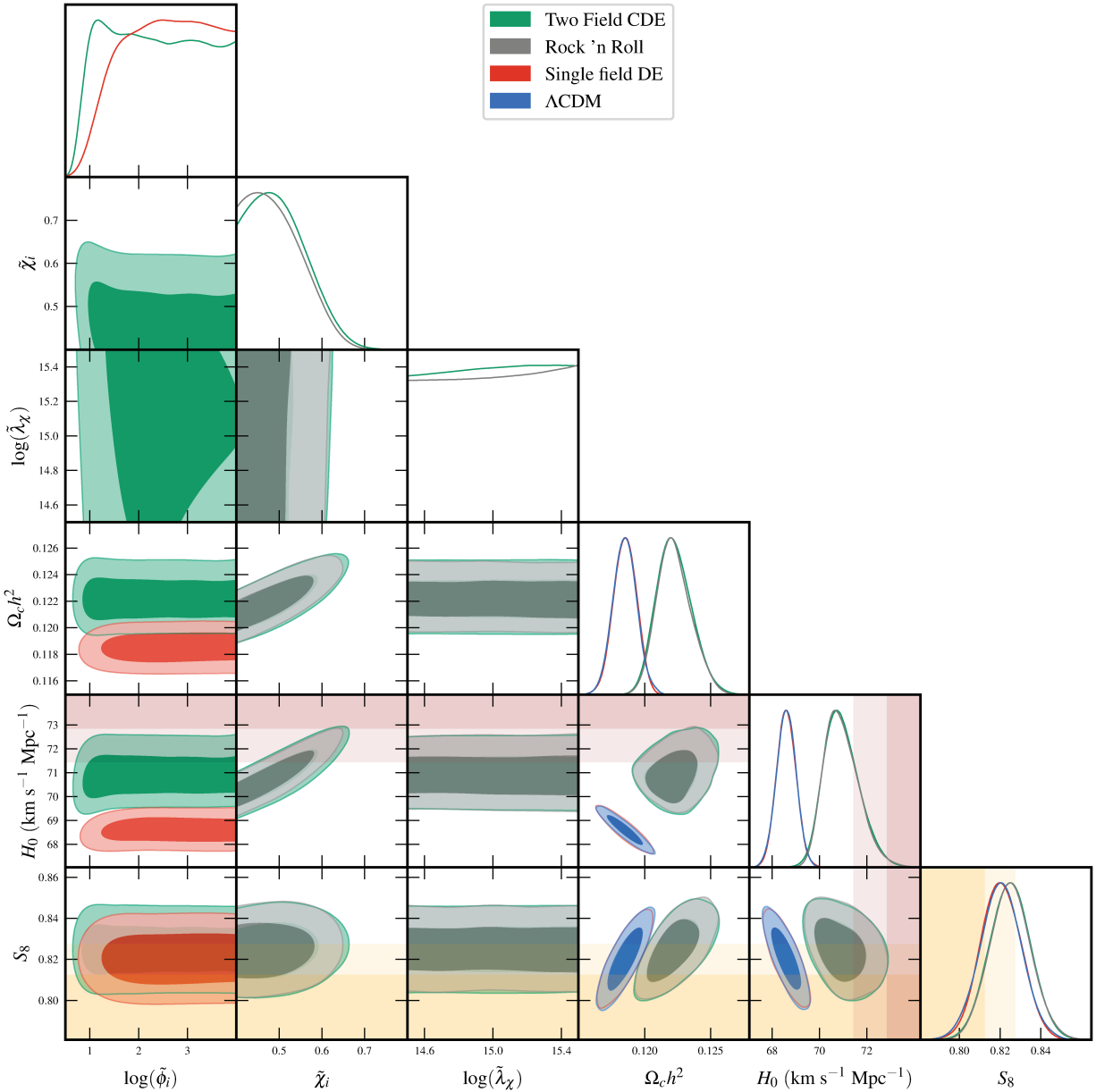


FIG. 1. 1D likelihoods and 2D contours for the parameters in 68% and 95% CL marginalized joint regions for the Λ CDM model (blue), the single-field DE model (red), the Rock ‘n’ Roll model (gray), and the two-field CDE model (green). The logarithms for $\tilde{\phi}_i$ and $\tilde{\lambda}_\chi$ are base 10. The shaded orange region (horizontal in the first 5 left bottom plot, vertical in the last bottom plot on the right) shows the allowed region for H_0 from Riess et al. (2019) [9]. The pink shaded region (horizontal for the first left 4 plots in the row of plots second from the bottom, vertical in the last plot on the right in the same row), shows the DES constraints to S_8 described in Ref. [54].

model fits the CMB data slightly better than the two-field CDE model, but the two-field scenario performs better in fitting the PANTHEON data.

An interesting feature of the two-field CDE model is that it provides a better fit to the BAO data in comparison with the Rock ‘n’ Roll model which implies that BAO data, showing some preference for late-time evolution in the DE component. Altogether, the table shows that

the two-field CDE model provides the minimum value of χ^2_{total} . From Table II, we conclude that in our two-field CDE scenario, $\Delta\chi^2$ gets reduced relative to Λ CDM, single-field DE, and Rock ‘n’ Roll by 7.17, 7.31, and 0.66, respectively.

Results for 1D likelihoods and 2D contour plots in the 68% and 95% CL regions are shown in Fig. 1. The graph indicates that the results of the single-field DE model are

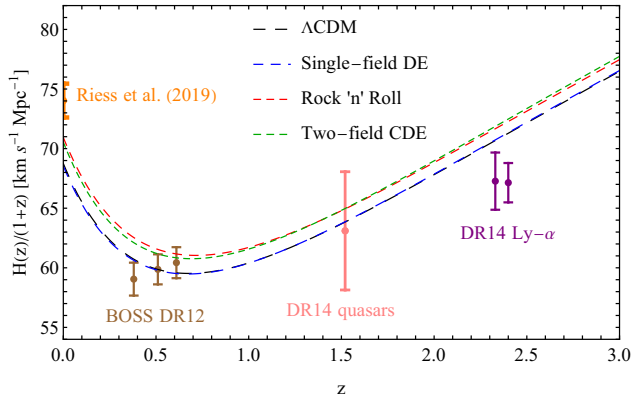


FIG. 2. Evolution of the $H(z)/(1+z)$ as a function of cosmological redshift in the Λ CDM, single-field DE, Rock ‘n’ Roll and two-field CDE models. Also, in the figure, the data-points from the Riess et al. (2019) [9], BOSS DR12 [39], DR14 quasars [84], and DR14 Ly- α [85] measurements have been specified for comparison.

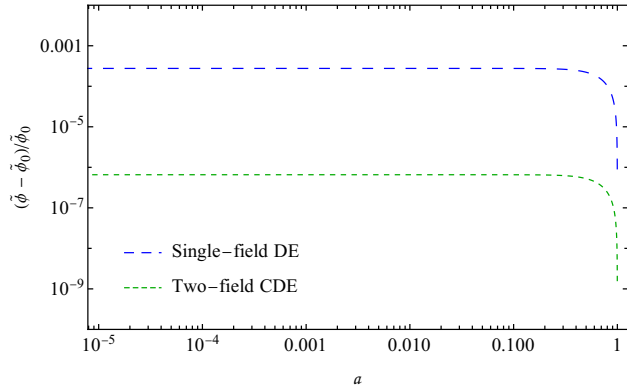


FIG. 3. Evolution of the scalar field $\tilde{\phi}$ as a function of scale factor in the single-field DE and two-field CDE models.

very close to those of the Λ CDM model, and also the results of the two-field CDE model are very close to the Rock ‘n’ Roll results.

The two-field CDE and Rock ‘n’ Roll models provide higher values for the H_0 parameter relative to the Λ CDM and single-field DE models, and therefore mitigate the Hubble tension. The 2D contour plots of the two-field CDE and Rock ‘n’ Roll models which include the H_0 parameter, are separated thoroughly from the contour plots of the Λ CDM and single-field DE models. This reinforces the fact that the Hubble tension can be alleviated in models which invoke some type of energy injection before recombination in the past evolution of the Universe. Nevertheless, the two-field CDE and Rock ‘n’ Roll scenarios yield greater values for the S_8 parameter, and so these models worsen the LSS tension in comparison with the Λ CDM and single-field DE settings, as already noted.

The value of τ , the optical depth parameter, decreases with respect to the Λ CDM and single field DE scenario in our CDE model. In the two-field CDE model, the

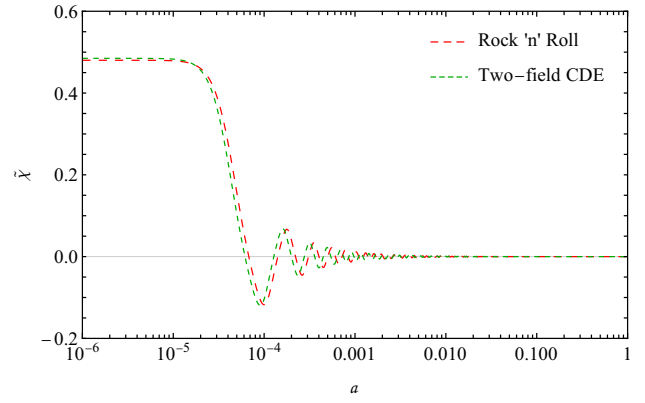


FIG. 4. Evolution of the scalar field $\tilde{\chi}$ as a function of scale factor in the Rock ‘n’ Roll and two-field CDE models.

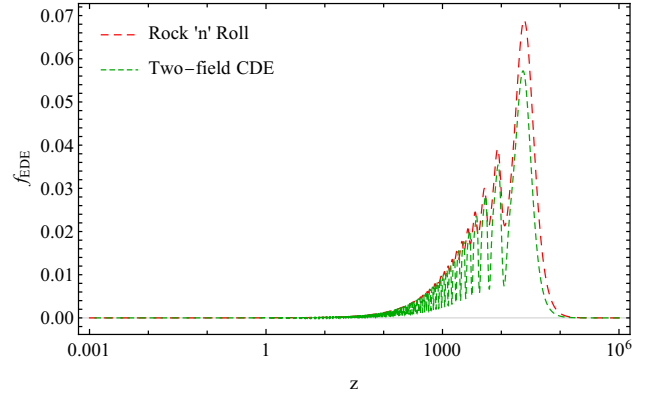


FIG. 5. Evolution of the f_{EDE} as a function of cosmological redshift in the Rock ‘n’ Roll and two-field CDE models.

value of this parameter gets reduced slightly more. In contrast to Ref. [15], the amplitude of the best fit scalar power spectrum is enhanced in the Rock ‘n’ Roll mode in comparison with the Λ CDM, while the scalar spectral index gets reduced. In the two-field CDE though, both the amplitude of power spectrum and scalar spectral index are enhanced with respect to Λ CDM. We see in

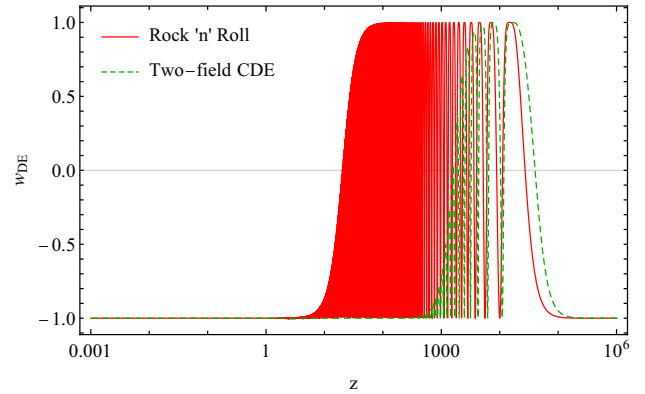


FIG. 6. Evolution of the w_{DE} as a function of cosmological redshift in the Rock ‘n’ Roll and two-field CDE models.

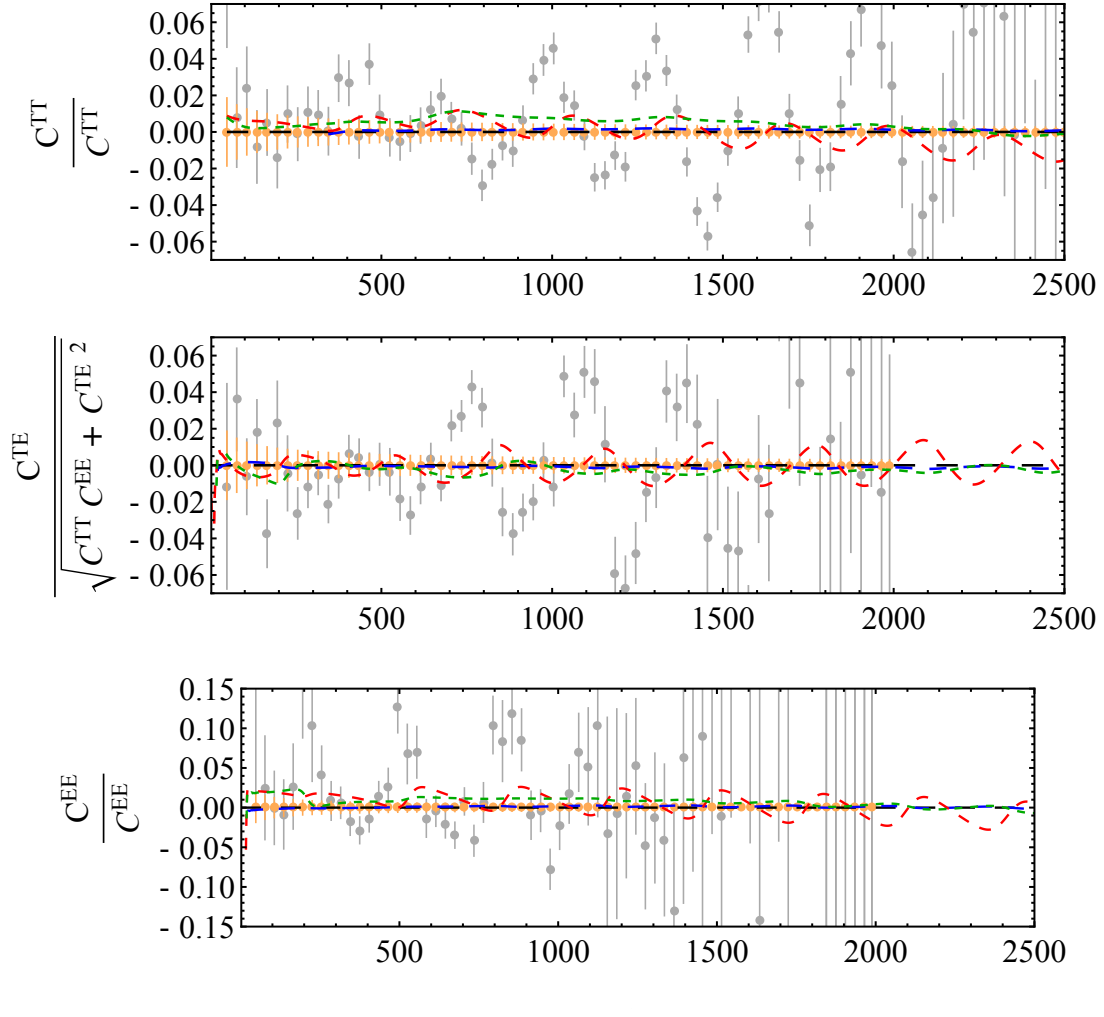


FIG. 7. Residuals of the binned CMB power spectra relative to the reference Λ CDM model. The results of the Λ CDM (dashed black), single-field DE (dashed blue), Rock ‘n’ Roll (dashed red), and two-field CDE (dashed green) are compared with the binned Planck 2018 data-points (gray) [5–7]. Fractional errors for a cosmic-variance-limited experiment are shown in orange. We compared models using the best-fit parameters for all cases.

Fig. 1 that the two-field CDE and Rock ‘n’ Roll models prefer smaller values for Ω_m than the Λ CDM and single-field DE scenarios, a common property of EDE scenarios [13, 17, 45–47].

Figure 1 additionally shows that the likelihood is quite insensitive to ϕ_i and λ_χ , as evidenced by the flatness of the posterior contours in these parameters. Despite this, there is a preferred value for $\tilde{\chi}_i$ in the two-field CDE and Rock ‘n’ Roll models. This fact implies that our numerical analysis prefers a non-vanishing contribution of EDE to the cosmic energy density.

In Fig. 2, we used the best fit values of the parameters listed in Table I to plot the evolution of the Hubble parameter against of redshift, showing that the Hubble parameter of the single-field DE model is very similar to Λ CDM. Also, the results of the Rock ‘n’ Roll and two-field CDE models are very close to each other. Nevertheless, at earlier times, the Hubble parameter of the two-field CDE model is above the one for the Rock ‘n’

Roll scenario, but at late times, the Rock ‘n’ Roll Hubble parameter takes larger values, so this model gives a greater H_0 .

Smaller values of the Hubble parameter at lower redshifts give better compatibility of the two-field CDE model with BAO data, compared to Rock ‘n’ Roll. Simultaneous agreement with PANTHEON and BAO data causes the ϕ field to be over-constrained by the data, limiting the ability of the CDE model to better fit BAO data. It may be possible to go beyond this limitation by adding additional scalar fields. We have also developed a modified version of CAMB that has **three** dynamical fields (χ , ϕ , and a field ξ that rolls at an intermediate redshift). By trial and error, we have found that there are combinations of initial field values and coupling constants that provide a significantly better fit to lower- z BAO data (e.g. as in Fig. 2). In future work, we will extend our MCMC analysis to this richer scenario.

In Fig. 3, we show the evolution of the normalized

scalar field $\tilde{\phi}$ in the single-field DE and two-field CDE models as a function of scale factor. Aside from a small interval at late times, the scalar field $\tilde{\phi}$ tends to remain constant. But, around the present epoch, it becomes dynamical. The fractional variation of $\tilde{\phi}$ in the (best-fitting) single-field scenario is substantially greater than in the (best-fitting) two-field CDE scenario - this is because simultaneously allowing late and early-time dark energy allows the model to fit both the late-time acceleration of the Universe and provide the required early-time reduction in the sound horizon needed to resolve the Hubble tension. In some sense, demanding less of the ϕ field allows its late-time behavior to more closely resemble Λ CDM.

In Fig. 4, the evolution of the scalar field $\tilde{\chi}$ as a function of scale factor is plotted for the Rock ‘n’ Roll and two-field CDE setups. Here we have used the best fit values given in Table I. The figure displays that the scalar field $\tilde{\chi}$ is almost constant at earlier times in these models, and after a period of time, it begins to oscillate around the potential minimum at $\tilde{\chi} = 0$. The initial value of $\tilde{\chi}$ is bigger in the two-field CDE model compared to the Rock ‘n’ Roll model, and also its oscillations occur in this model earlier than in the Rock ‘n’ Roll model. At late times, the amplitude of the $\tilde{\chi}$ oscillations becomes very small, and accordingly, its contribution to the matter-energy content of the Universe becomes negligible.

In Fig. 5, we show the fraction of the EDE energy density relative to the total energy density, that is, $f_{\text{EDE}} \equiv \rho_{\chi}/\rho_{\text{total}}$. We see that f_{EDE} is negligible at the initial times, but after a while, it grows sharply and reaches a peak at the critical redshift z_c , and then it drops again and becomes very small at the late-times. For the Rock ‘n’ Roll model, the peak appears at the critical redshift $z_c = 2.44 \times 10^4$ with the maximum value $f_{\text{EDE}} = 0.069$. The peak of the two-field CDE model appears at $z_c = 2.34 \times 10^4$ with the maximum amplitude $f_{\text{EDE}} = 0.057$.

Figure 6 shows the evolution of the equation of state parameter of dark energy, $w_{\text{DE}} \equiv p_{\text{DE}}/\rho_{\text{DE}} = (p_{\phi} + p_{\chi})/(\rho_{\phi} + \rho_{\chi})$, in terms of cosmological redshift. At high redshifts, w_{DE} begins at -1 , and subsequently oscillates around zero, with w_{DE} varying between -1 and 1 . Eventually, it converges to -1 and remains very close to this value until the present time. The oscillations of w_{DE} start sooner in the two-field CDE model than in the Rock ‘n’ Roll scenario, although the oscillations last longer for Rock ‘n’ Roll.

We present the residuals of CMB power spectra in Fig. 7. In the figure, we have also shown Planck 2018 data points [5–7] for comparison. We see in the figure that the results of the single-field DE are indistinguishable from Λ CDM results, while the Rock ‘n’ Roll and two-field CDE models show deviations from Λ CDM, exceeding cosmic variance in some cases. To roughly estimate the improvement in constraining power of future CMB

experiments, we compute the statistic [86]

$$\mathcal{Z} \equiv \sqrt{\sum_{\ell} \frac{\Delta C_{\ell}^2}{\sigma_{\ell}^2}}, \quad (41)$$

where the sum over the binned spectrum is evaluated using the deviation ΔC_{ℓ} of the model of interest, with binned cosmic variance errors used for σ_{ℓ} . We separately compute this sum for temperature and EE polarization. A full forecast requires a proper analysis of T and E covariances, or better yet, a full Fisher matrix analysis that properly accounts for parameter degeneracies including nuisance parameters). Nonetheless, this rough estimate can give us some sense of whether or not the CMB alone can detect deviations between the models we consider, with future data. Roughly speaking, \mathcal{Z} is the number of sigmas at which two scenarios can be distinguished.

Using temperature, we find that future data could distinguish between the single and two-field scenarios with $\sim 3\sigma$ significance, which improves to a $\sim 20\sigma$ potential detection in the limit that TE covariances vanish. Of course, this is not the case, and so a full Fisher matrix forecast is likely to show an answer closer to $\sim 7\sigma$ (ie, the geometric mean of the two extreme cases).

The predictions of the Rock ‘n’ Roll model match the CMB data better than the other models, and provide the best fit to CMB data of the models considered in this work, as also shown in Table II. The better consistency of this model with the observational data points is more apparent at low ℓ s, $\ell \sim 700$, $\ell \sim 1000$, and also high ℓ s. The two-field CDE model displays the next best agreement with CMB data.

V. CONCLUSIONS

We studied the cascading dark energy model, in which many scalar fields contribute to the dark energy component of the Universe. In this setup, a large number of canonical scalar fields with sub-Planckian field excursions and steep potentials cooperate to provide a super-Planckian excursion and a relatively flat potential that can induce the late acceleration of the Universe as well as an early dark energy epoch. In the example we considered, the discordant initial conditions between fields cause some to cascade, drop out of the ensemble, and start oscillating around their minima. We restricted our attention to a single cascade involving an interplay reducing to an effective theory of two fields, ϕ , and χ . We choose the initial conditions such that ϕ plays the role of the late dark energy, while χ field behaves as EDE, subsequently cascading and decaying quickly.

We used MCMC simulations to test CDE and related scenarios using CMB, BAO, PANTHEON observations of Type-Ia supernovae, and Riess et al. (2019) data. Our work shows that $\Delta\chi^2$ gets reduced relative to Λ CDM, single-field DE, and Rock ‘n’ Roll by 7.17, 7.31, and 0.66, respectively. The two-field CDE model yields

a fit of $H_0 = 70.95^{+0.61}_{-0.85} \text{ km s}^{-1}\text{Mpc}^{-1}$, substantially higher than ΛCDM ($H_0 = 68.60 \pm 0.41 \text{ km s}^{-1}\text{Mpc}^{-1}$) and single-field DE ($H_0 = 68.60 \pm 0.41 \text{ km s}^{-1}\text{Mpc}^{-1}$) values, while very close to the Rock ‘n’ Roll values ($H_0 = 70.94^{+0.58}_{-0.84} \text{ km s}^{-1}\text{Mpc}^{-1}$). The CDE and Rock ‘n’ Roll versions of the EDE scenario thus reduce the Hubble tension between supernovae ($H_0 = 74.03 \pm 1.42 \text{ km s}^{-1}\text{Mpc}^{-1}$) and other methods. Our analysis also shows that the two-field CDE model ($\chi^2_{\text{BAO}} = 6.61057$) provides a modestly improved fit to BAO data compared with the Rock ‘n’ Roll model ($\chi^2_{\text{BAO}} = 8.63314$).

There are a number of important avenues needed to expand and critically test our results. The analysis shown here did not follow the linear perturbations of either DE component - as noted, these do have a statistical impact on inferences about EDE properties, and in the future, we will generalize our analysis to include CDE clustering in the linear regime. We will also explore the possibility of rich resonant non-linear phenomenology, as discussed in Refs. [17]. Another area for future work is the exploration of a broader range of potential energy functions, motivated by a variety of considerations.

Since the effective super-Planckian field samples the potential at relatively large values of the scalar field, the form of the potential at such values of the field can effectively be different from the part of the potential that only samples the sub-Planckian values of the field. For example, the late field can effectively be on the parts

of the potential that is just a cosmological constant. In this limit, the predictions and statistical significance of the model should be comparable approaches to the Rock ‘n’ Roll model. However, in principle, the late and early dark energy fields can have different potentials and this affects the predictions of the model. This is one interesting research avenue that is worth considering in the future.

Even with monomial potentials for both the late and early dark energy fields, one can assume non-renormalizable forms for the potentials. For example with a sixth-order monomial potential, ϕ^6 , we expect that the model can achieve larger values of H_0 . The scalar fields also may have non-canonical kinetic terms. In particular, we can consider the DBI kinetic terms which have well-based theoretical motivations. In addition, although in this paper, we assumed that the late dark energy and the cascading fields couple to the Einstein gravity minimally, one can consider their non-minimal couplings with gravity too. These possibilities are left for future investigations.

ACKNOWLEDGMENTS

D. G. acknowledges support in part by NASA ATP Grant No. 17-ATP17-0162, and the provost’s office of Haverford College. We thank Tristan Smith for useful conversations.

-
- [1] A. G. Riess et al., *Astrophys. J.* **826**, 56 (2016).
 - [2] A. G. Riess et al., *Astrophys. J.* **861**, 126 (2018).
 - [3] V. Bonvin et al., *Mon. Not. Roy. Astron. Soc.* **465**, 4914 (2017).
 - [4] S. Birrer et al., *Mon. Not. Roy. Astron. Soc.* **484**, 4726 (2019).
 - [5] N. Aghanim et al., *Astron. Astrophys.* **641**, A6 (2020), [Erratum: *Astron. Astrophys.* 652, C4 (2021)].
 - [6] N. Aghanim et al., *Astron. Astrophys.* **641**, A5 (2020).
 - [7] N. Aghanim et al., *Astron. Astrophys.* **641**, A8 (2020).
 - [8] T. M. C. Abbott et al., *Mon. Not. Roy. Astron. Soc.* **480**, 3879 (2018).
 - [9] A. G. Riess, S. Casertano, W. Yuan, L. M. Macri, and D. Scolnic, *Astrophys. J.* **876**, 85 (2019).
 - [10] C. Umiltà, M. Ballardini, F. Finelli, and D. Paoletti, *JCAP* **08**, 017 (2015).
 - [11] T. Karwal and M. Kamionkowski, *Phys. Rev. D* **94**, 103523 (2016).
 - [12] V. Poulin, T. L. Smith, D. Grin, T. Karwal, and M. Kamionkowski, *Phys. Rev. D* **98**, 083525 (2018).
 - [13] V. Poulin, T. L. Smith, T. Karwal, and M. Kamionkowski, *Phys. Rev. Lett.* **122**, 221301 (2019).
 - [14] K. L. Pandey, T. Karwal, and S. Das, *JCAP* **07**, 026 (2020).
 - [15] P. Agrawal, F.-Y. Cyr-Racine, D. Pinner, and L. Randall, (2019).
 - [16] S. Vagnozzi, *Phys. Rev. D* **102**, 023518 (2020).
 - [17] T. L. Smith, V. Poulin, and M. A. Amin, *Phys. Rev. D* **101**, 063523 (2020).
 - [18] Z. Davari, V. Marra, and M. Malekjani, *Mon. Not. Roy. Astron. Soc.* **491**, 1920 (2020).
 - [19] J. Sola, A. Gomez-Valent, J. d. C. Perez, and C. Moreno-Pulido, *Class. Quant. Grav.* **37**, 245003 (2020).
 - [20] T. L. Smith et al., (2020).
 - [21] C. Krishnan, E. O. Colgain, M. Sheikh-Jabbari, and T. Yang, (2020).
 - [22] E. Di Valentino, A. Melchiorri, and J. Silk, *Phys. Lett. B* **761**, 242 (2016).
 - [23] E. Di Valentino, A. Melchiorri, E. V. Linder, and J. Silk, *Phys. Rev. D* **96**, 023523 (2017).
 - [24] E. Di Valentino, E. V. Linder, and A. Melchiorri, *Phys. Rev. D* **97**, 043528 (2018).
 - [25] S. Kumar and R. C. Nunes, *Phys. Rev. D* **94**, 123511 (2016).
 - [26] E. Di Valentino, A. Melchiorri, and O. Mena, *Phys. Rev. D* **96**, 043503 (2017).
 - [27] A. Barreira, B. Li, C. Baugh, and S. Pascoli, *JCAP* **08**, 059 (2014).
 - [28] M. Ballardini, F. Finelli, C. Umiltà, and D. Paoletti, *JCAP* **05**, 067 (2016).
 - [29] J. Renk, M. Zumalacárregui, F. Montanari, and A. Barreira, *JCAP* **10**, 020 (2017).

- [30] E. Belgacem, Y. Dirian, S. Foffa, and M. Maggiore, *JCAP* **03**, 002 (2018).
- [31] R. C. Nunes, *JCAP* **05**, 052 (2018).
- [32] M.-X. Lin, M. Raveri, and W. Hu, *Phys. Rev. D* **99**, 043514 (2019).
- [33] G. E. Addison et al., *Astrophys. J.* **853**, 119 (2018).
- [34] J. L. Bernal, L. Verde, and A. G. Riess, *JCAP* **10**, 019 (2016).
- [35] G.-B. Zhao et al., *Nature Astron.* **1**, 627 (2017).
- [36] V. Poulin, K. K. Boddy, S. Bird, and M. Kamionkowski, *Phys. Rev. D* **97**, 123504 (2018).
- [37] F. Beutler et al., *Mon. Not. Roy. Astron. Soc.* **416**, 3017 (2011).
- [38] A. J. Ross et al., *Mon. Not. Roy. Astron. Soc.* **449**, 835 (2015).
- [39] S. Alam et al., *Mon. Not. Roy. Astron. Soc.* **470**, 2617 (2017).
- [40] G. Efstathiou, *Mon. Not. Roy. Astron. Soc.* **505**, 3866 (2021).
- [41] R. Jimenez, A. Cimatti, L. Verde, M. Moresco, and B. Wandelt, *JCAP* **03**, 043 (2019).
- [42] D. Valcin, J. L. Bernal, R. Jimenez, L. Verde, and B. D. Wandelt, *JCAP* **12**, 002 (2020).
- [43] D. Valcin, R. Jimenez, L. Verde, J. L. Bernal, and B. D. Wandelt, *JCAP* **08**, 017 (2021).
- [44] J. L. Bernal et al., *Phys. Rev. D* **103**, 103533 (2021).
- [45] T. Karwal, M. Raveri, B. Jain, J. Khoury, and M. Trodden, *Phys. Rev. D* **105**, 063535 (2022).
- [46] V. Poulin, T. L. Smith, and A. Bartlett, *Phys. Rev. D* **104**, 123550 (2021).
- [47] R. Murgia, G. F. Abellán, and V. Poulin, *Phys. Rev. D* **103**, 063502 (2021).
- [48] T. M. C. Abbott et al., *Phys. Rev. D* **98**, 043526 (2018).
- [49] H. Hildebrandt et al., *Astron. Astrophys.* **633**, A69 (2020).
- [50] C. Hikage et al., *Publ. Astron. Soc. Jap.* **71**, 43 (2019).
- [51] M. Asgari et al., *Astron. Astrophys.* **645**, A104 (2021).
- [52] H. Hildebrandt, *PoS EPS-HEP2017*, 039 (2017).
- [53] T. M. C. Abbott et al., *Phys. Rev. D* **105**, 023520 (2022).
- [54] D. Zürcher et al., *Monthly Notices of the Royal Astronomical Society* **511**, 2075 (2022).
- [55] J. C. Hill, E. McDonough, M. W. Toomey, and S. Alexander, *Phys. Rev. D* **102**, 043507 (2020).
- [56] M. M. Ivanov et al., *Phys. Rev. D* **102**, 103502 (2020).
- [57] F. Niedermann and M. S. Sloth, *Phys. Rev. D* **103**, L041303 (2021).
- [58] F. Niedermann and M. S. Sloth, *Phys. Rev. D* **105**, 063509 (2022).
- [59] K. Freese and M. W. Winkler, *Phys. Rev. D* **104**, 083533 (2021).
- [60] I. J. Allali, M. P. Hertzberg, and F. Rompineve, *Phys. Rev. D* **104**, L081303 (2021).
- [61] V. I. Sabla and R. R. Caldwell, *Phys. Rev. D* **103**, 103506 (2021).
- [62] A. R. Liddle, A. Mazumdar, and F. E. Schunck, *Phys. Rev. D* **58**, 061301 (1998).
- [63] C. Vafa, (2005).
- [64] H. Ooguri and C. Vafa, *Nucl. Phys. B* **766**, 21 (2007).
- [65] G. Obied, H. Ooguri, L. Spodyneiko, and C. Vafa, (2018).
- [66] A. Arvanitaki, S. Dimopoulos, S. Dubovsky, N. Kaloper, and J. March-Russell, *Phys. Rev. D* **81**, 123530 (2010).
- [67] R. Hlozek, D. Grin, D. J. E. Marsh, and P. G. Ferreira, *Phys. Rev. D* **91**, 103512 (2015).
- [68] D. J. E. Marsh, *Phys. Rept.* **643**, 1 (2016).
- [69] M. Kamionkowski, J. Pradler, and D. G. E. Walker, *Phys. Rev. Lett.* **113**, 251302 (2014).
- [70] R. Emami, D. Grin, J. Pradler, A. Raccanelli, and M. Kamionkowski, *Phys. Rev. D* **93**, 123005 (2016).
- [71] D. M. Scolnic et al., *Astrophys. J.* **859**, 101 (2018).
- [72] F. Beutler et al., *Mon. Not. Roy. Astron. Soc.* **423**, 3430 (2012).
- [73] A. Lewis and S. Bridle, *Phys. Rev. D* **66**, 103511 (2002).
- [74] A. Lewis, (2019).
- [75] A. Ashoorioon, H. Firouzjahi, and M. M. Sheikh-Jabbari, *JCAP* **05**, 002 (2010).
- [76] A. Ashoorioon, H. Firouzjahi, and M. M. Sheikh-Jabbari, *JCAP* **06**, 018 (2009).
- [77] A. Ashoorioon and M. M. Sheikh-Jabbari, *JCAP* **06**, 014 (2011).
- [78] A. Ashoorioon and M. M. Sheikh-Jabbari, *Phys. Lett. B* **739**, 391 (2014).
- [79] A. Ashoorioon and K. Rezazadeh, *JHEP* **07**, 244 (2020).
- [80] K. Rezazadeh, S. Asadzadeh, K. Fahimi, K. Karami, and A. Mehrabi, *Annals Phys.* **422**, 168299 (2020).
- [81] P. A. R. Ade et al., *Astron. Astrophys.* **571**, A16 (2014).
- [82] W. Hu and N. Sugiyama, *Astrophys. J.* **471**, 542 (1996).
- [83] A. Gelman and D. B. Rubin, *Statist. Sci.* **7**, 457 (1992).
- [84] P. Zarrouk et al., *Mon. Not. Roy. Astron. Soc.* **477**, 1639 (2018).
- [85] M. Blomqvist et al., *Astron. Astrophys.* **629**, A86 (2019).
- [86] D. Grin and C. M. Hirata, *Phys. Rev. D* **81**, 083005 (2010).